Received: 19 June 2017 | Revised: 16 October 2017 | Accepted: 3 December 2017

DOI: 10.1002/fld.4482

RESEARCH ARTICLE

WILEY

The improvement of numerical modeling in the solution of incompressible viscous flow problems using finite element method based on spherical Hankel shape functions

Sajedeh Farmani | Mahnaz Ghaeini-Hessaroeyeh | Saleh Hamzehei Javaran

Department of Civil Engineering, Faculty of Engineering, Shahid Bahonar University of Kerman, Kerman, Iran

Correspondence
Mahnaz Ghaeini-Hessaroeyeh, Department of Civil Engineering, Faculty of Engineering, Shahid Bahonar University of Kerman, Kerman 76169 133, Iran.
Email: mghaeini@uk.ac.ir; mahnaz.ghaeini@gmail.com

Summary

In this paper, the finite element method with new spherical Hankel shape functions is developed for simulating 2-dimensional incompressible viscous fluid problems. In order to approximate the hydrodynamic variables, the finite element method based on new shape functions is reformulated. The governing equations are the Navier-Stokes equations solved by the finite element method with the classic Lagrange and spherical Hankel shape functions. The new shape functions are derived using the first and second kinds of Bessel functions. In addition, these functions have properties such as piecewise continuity. For the enrichment of Hankel radial basis functions, polynomial terms are added to the functional expansion that only employs spherical Hankel radial basis functions in the approximation. In addition, the participation of spherical Bessel function fields has enhanced the robustness and efficiency of the interpolation. To demonstrate the efficiency and accuracy of these shape functions, 4 benchmark tests in fluid mechanics are considered. Then, the present model results are compared with the classic finite element results and available analytical and numerical solutions. The results show that the proposed method, even with less number of elements, is more accurate than the classic finite element method.

KEYWORDS

classic Lagrange shape functions, finite element method, hydrodynamic variables, incompressible viscous fluids, Navier-Stokes equations, spherical Hankel shape functions

1 | INTRODUCTION

Fluid mechanics is one of the fields of physics related to the statics and dynamics of fluids and also their effect on their surroundings. If the variation of fluid density is neglected, the fluid is considered incompressible. The governing equations of incompressible viscous fluids are conservation of mass and momentum (Navier-Stokes equations[1]). To solve these equations, the analytical methods and numerical ones can be used. However, many of the problems cannot be solved by the analytical method or the analytical solution is too complicated. Therefore, various numerical methods are developed for solving these equations with acceptable accuracy.

In general, there are 2 viewpoints in the fluid mechanics: Lagrangian and Eulerian. In the first one, the computational domain is divided into some moving particles. In other words, this approach does not need to be meshed. Moving-particle semi-implicit method, smoothed particle hydrodynamics method, element-free Galerkin method, and

discrete least-squares meshless method are examples of Lagrangian approaches. In the second approach, the computational domain is divided into some elements or the so-called meshes. Then, the governing equations are solved on the grid. This approach includes a finite element method (FEM), a finite difference method, and a finite volume method. This paper focuses on the FEM based on the mesh.

The FEM is a technique that has a particular ability in handling very complex geometry and applying the differential-type boundary conditions. Some researchers studied on solving the Navier-Stokes equations using FEM. Reddy,[1] Zienkiewicz,[2] Hood,[3] Oden,[4] and Taylor and Hood[5] were the people who attempted to solve these equations by FEM. In this field, Hughes et al[6] presented a review of an incompressible viscous flow analysis by a penalty finite element approach. Souli and Zolesio[7] introduced a numerical method for solving incompressible irrotational and inviscid flow with a free surface. The linear stability of incompressible flows is investigated based on FEM by Ding and Kawahara.[8]

Furthermore, the incompressible viscous flows based on meshless methods are studied by some researchers. Basa et al[9] investigated the robustness and accuracy of smoothed particle hydrodynamics formulation for viscous incompressible flows. You et al[10] simulated the viscous incompressible flows using an element-free Galerkin method.

In the incompressible viscous flow problems, the unknowns include velocity in the x-direction (v_x), velocity in the y-direction (v_y), and pressure (p). In this paper, the mixed finite element approach, in which an element contains variable degrees of freedom, is used. For example, for the 9-node element, there are 3 degrees of freedom (v_x, v_y, and p) at the corner nodes and 2 degrees of freedom (v_x and v_y) at the midside and interior nodes. This problem complicates the calculation of element matrices, as well as the assembly of element equations. Therefore, this problem increases CPU time and storage space.[1] In addition, for some complicated problems, it is necessary to use elements with ultrasmall dimensions. This matter leads to having a higher number of unknowns, and as a result, the computational effort and cost increase. Therefore, in this research, it is tried to improve the accuracy of modeling incompressible viscous flow problems using a new set of shape functions. By these functions, the degrees of freedom decrease and, then, the computational cost is also reduced.

In the present model, a new set of shape functions derived from a spherical Hankel radial basis function (RBF) is proposed and reformulated. In general, RBFs are used for the approximation of multivariable functions by the linear combination of terms depending on a univariate function, which is called RBF.[11] There are 2 types of RBFs called oscillatory and nonoscillatory. The conical functions,[12-14] the thin plate spline,[15-17] the Gaussian functions,[18] multiquadrics,[19,20] inverse multiquadrics,[21] and compact supported functions[22-25] are placed in a nonoscillatory class, whereas real and complex Fourier RBF[26-28] and J-Bessel RBF[29] are in the oscillatory category. In classical mathematics, Fourier-Bessel series and J-Bessel RBFs are applied as basis functions. The J-Bessel RBF only includes the features of the Bessel function of the first kind, whereas in most cases, the first kind of Bessel function cannot express the full properties of a physical phenomenon. In order to have both properties of the first and second kinds of Bessel function, the Hankel shape functions are applied in the present model. In the field of using these shape functions, Hamzehei Javaran and Shojaee[30] improved the accuracy of the boundary element method in solving elastostatic and elastodynamic problems. They achieved very good results with a few number of elements.

In this research, at first, the governing equations of the viscous incompressible flow are expressed. Then, the discretization of these equations is developed based on the FEM. In addition, the proposed shape functions for a Hankel element with 9 nodes have been derived. Finally, for evaluating the results of the proposed method, some tests in fluid mechanics are selected. These tests are simulated by the present model. The results are analyzed by the standard FEM and RBF based on spherical Hankel shape functions with a few number of elements. In addition, both series of the present model results are compared with the available analytical and numerical solutions. Then, the efficiency of the proposed shape functions is examined.

2 | GOVERNING EQUATIONS

The behavior of viscous incompressible flow can be represented by the Navier-Stokes equations. These equations include the conservation of mass and momentum that are described as follows by relations (1) and (2), respectively[1]:

$$\nabla.\mathbf{v} = 0 \tag{1}$$

$$\rho\left(\frac{\partial \mathbf{v}}{\partial t} + \mathbf{v}.\nabla\mathbf{v}\right) = \nabla.\sigma + \rho\mathbf{f}, \tag{2}$$

where $\mathbf{v}$ denotes the velocity, ∇ is the vector differential operator, ρ represents the fluid density, σ indicates the stress tensor, and $\mathbf{f}$ implies the body force vector.

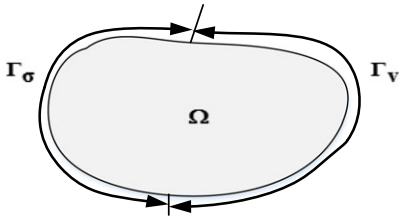

FIGURE 1 A schematic of the boundary condition related to velocity and traction

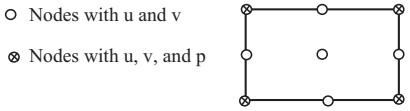

FIGURE 2 The element used for the viscous incompressible flow in the present model

3 | BOUNDARY CONDITIONS

The boundary conditions are given by the following relations[31]:

$$\mathbf{v} = \mathbf{f}^{v} \quad \text{on} \quad \Gamma_{v} \tag{3a}$$

$$\tau \equiv \sigma.\mathbf{n} = \mathbf{f}^{\tau} \quad \text{on} \quad \Gamma_{\sigma}, \tag{3b}$$

where $\mathbf{n}$ is the unit normal vector to the boundary, and Γ_v and Γ_σ are the boundaries related to the velocity and traction, respectively, which are shown in Figure 1.[1] Dirichlet or essential boundary conditions are described by Equation (3a), and Neumann or natural boundary conditions are expressed by Equation (3b).[1]

4 | FEM FORMULATIONS OF INCOMPRESSIBLE VISCOUS FLOW PROBLEMS

By employing the FEM method in the Navier-Stokes equations, the final relation can be obtained as follows[1]:

$$\begin{bmatrix} [M] & [0] & [0] \\ [0] & [M] & [0] \\ [0] & [0] & [0] \end{bmatrix} \begin{Bmatrix} \dot{v}_x \\ \dot{v}_y \\ \dot{p} \end{Bmatrix} + \begin{bmatrix} 2[S^{xx}] + [S^{yy}] & [S^{yx}] & -[S^{x0}] \\ [S^{xy}] & [S^{xx}] + 2[S^{yy}] & -[S^{y0}] \\ -[S^{x0}]^T & -[S^{y0}]^T & [0] \end{bmatrix} \begin{Bmatrix} v_x \\ v_y \\ p \end{Bmatrix} + \begin{bmatrix} [C(\mathbf{v})] & [0] & [0] \\ [0] & [C(\mathbf{v})] & [0] \\ [0] & [0] & [0] \end{bmatrix} \begin{Bmatrix} v_x \\ v_y \\ p \end{Bmatrix} = \begin{Bmatrix} F^1 \\ F^2 \\ 0 \end{Bmatrix}. \tag{4}$$

Relation (4) is called *mixed finite element*. For more details of how to get the this equation, see the work of Reddy.[1] The coefficient matrices are written as follows[1]:

$$\begin{aligned} M_{ij} &= \int_{\Omega} \rho_0 \psi_i \psi_j dxdy \\ C_{ij}(\mathbf{v}) &= \int_{\Omega} \rho_0 \psi_i \left(v_x \frac{\partial \psi_j}{\partial x} + v_y \frac{\partial \psi_j}{\partial y} \right) dxdy \\ S_{ij}{}^{\zeta\eta} &= \int_{\Omega} \mu \left(\frac{\partial \psi_i}{\partial \zeta} \frac{\partial \psi_j}{\partial \eta} \right) dxdy; \zeta, \eta = x, y \\ S_{ij}{}^{\zeta 0} &= \int_{\Omega} \frac{\partial \psi_i}{\partial \zeta} \phi_j dxdy; \zeta = x, y \\ F^1 &= \int_{\Omega} \rho_0 \psi_i f_x dxdy + \oint_{\Gamma} \psi_i t_x ds \\ F^2 &= \int_{\Omega} \rho_0 \psi_i f_y dxdy + \oint_{\Gamma} \psi_i t_y ds, \end{aligned} \tag{5}$$

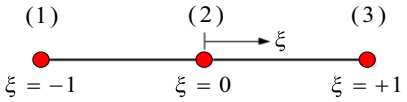

FIGURE 3 One-dimensional element with 3 nodes [Colour figure can be viewed at wileyonlinelibrary.com]

TABLE 1 Comparison of terms in classic Lagrange shape functions and spherical Hankel shape functions

Classic Lagrange Shape Functions	Spherical Hankel Shape Functions
$\frac{1}{2}(-\xi+1)$	$\frac{1}{2}\left(-\xi+\bar{c}+g(\xi)\right)$
$\frac{1}{2}(\xi+1)$	$\frac{1}{2}\left(\xi+\bar{c}+g(\xi)\right)$

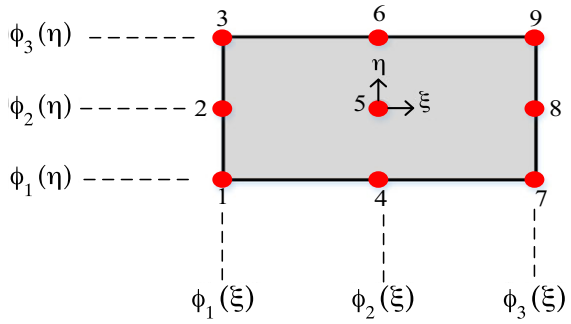

FIGURE 4 Two-dimensional element with 9 nodes [Colour figure can be viewed at wileyonlinelibrary.com]

where v_x and v_y are the velocity components in the x-direction and y-direction, respectively, p is the pressure, μ denotes the viscosity, and f_x and f_y are the components of the body force vector.

In addition, ψ and ϕ are considered as interpolation functions of velocity and pressure, respectively. t_x and t_y are the boundary stress components and are defined by the following relation[1]:

$$\begin{aligned} t_x &= \left(2\mu\frac{\partial v_x}{\partial x} - p\right) n_x + \mu\left(\frac{\partial v_x}{\partial y} + \frac{\partial v_y}{\partial x}\right) n_y \\ t_y &= \left(2\mu\frac{\partial v_y}{\partial y} - p\right) n_y + \mu\left(\frac{\partial v_x}{\partial y} + \frac{\partial v_y}{\partial x}\right) n_x, \end{aligned} \tag{6}$$

where n_x and n_y are the unit normal vectors in the x-direction and the y-direction, respectively.

The interpolation function of the pressure is different from the interpolation function of the velocity because there are the first derivatives of velocity, but there is no derivative of pressure in the weak form; see Equations (7)-(9). In addition, the essential boundary conditions do not contain the pressure and this variable belongs to the natural boundary conditions. Therefore, the used interpolation functions for the pressure variable should be 1 order less than those used for the velocity variables.

5 | CHOICE OF ELEMENT

The elements used in incompressible viscous flows should satisfy the Landyzhenskaya-Babuska-Brezzi condition.[32,33] By considering this condition, the quadrilateral elements (with 9 nodes for the velocity and 4 nodes for the pressure) are selected and shown in Figure 2.

6 | PROPOSED SHAPE FUNCTIONS

Radial basis functions are one of the approximation functions formed based on Euclidean norm. The RBFs introduced up to now, based on Bessel functions, just benefit from the first kind of Bessel function (J-Bessel), for example,

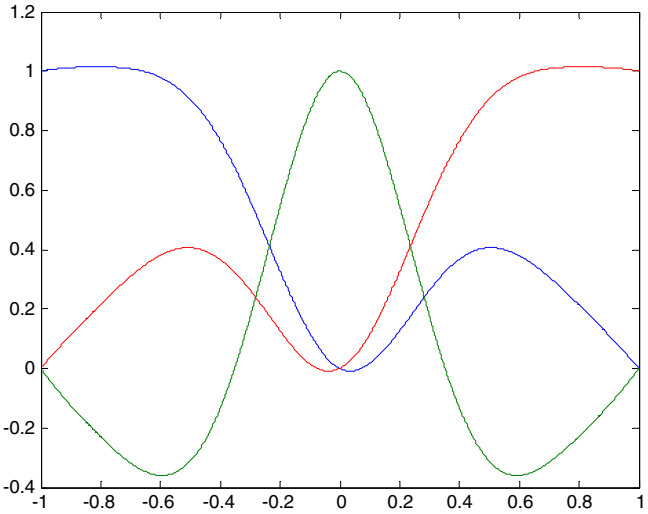

FIGURE 5 Spherical Hankel shape functions for a 3-node element when $\varepsilon = 6$ and $n = 1$ [Colour figure can be viewed at wileyonlinelibrary.com]

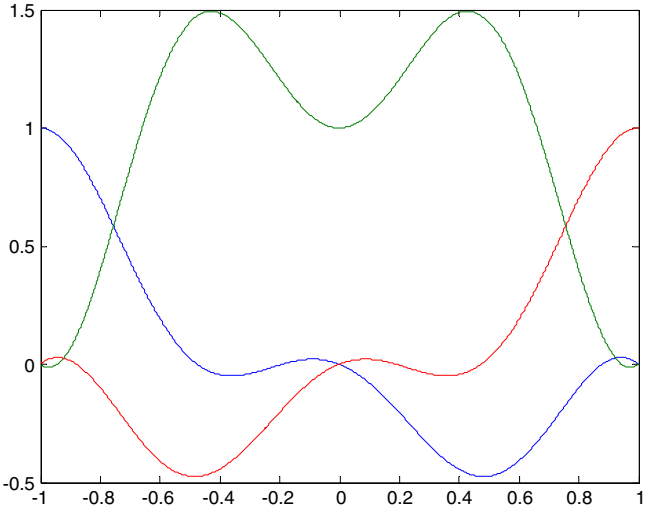

FIGURE 6 Spherical Hankel shape functions for a 3-node element when $\varepsilon = 6$ and $n = 3$ [Colour figure can be viewed at wileyonlinelibrary.com]

J-Bessel RBFs.[29] Generally, the Bessel equation of order z is expressed as follows:

$$x^2 y'' + xy' + \left(x^2 - z^2\right) y = 0, \tag{7}$$

which has a solution in the following form:

$$y = AJ_z + BY_z, \tag{8}$$

where A and B are constant, and J_z and Y_z denote the first and second kind of Bessel of order z, respectively. In most cases, the first kind of Bessel function cannot express the full properties of a physical phenomenon. For example, in solving the Bessel differential equation, the Neumann function is connected to the first kind by linear combination for obtaining a complete solution space. If the solution of the Bessel equation is obtained using the first and second kind of Bessel function, it is proved that the results can be better. A spherical Hankel function includes both Bessel functions of the first and second kind simultaneously. Therefore, the idea of using Hankel RBF in complex space is formed in this study, and its enrichment process is described in the following section.

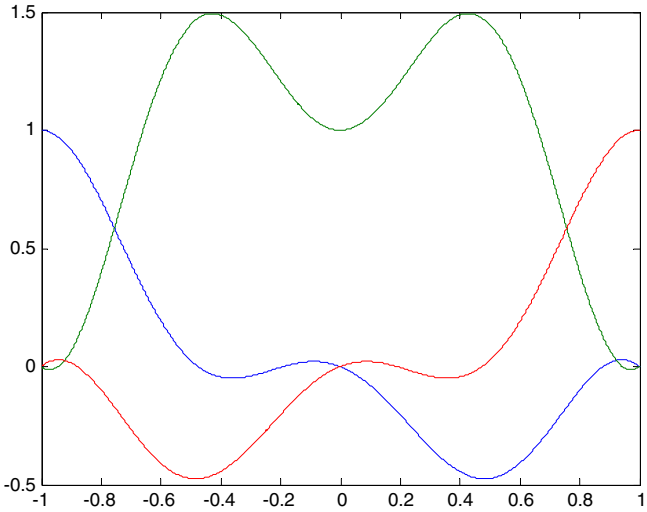

FIGURE 7 Spherical Hankel shape functions for a 3-node element when $\varepsilon = 6$ and $n = 6$ [Colour figure can be viewed at wileyonlinelibrary.com]

6.1 | Enrichment of spherical Hankel RBF

In this section, the steps for enrichment of Hankel RBF are expressed for a 3-node element, and then, it is extended for a 9-node element. Therefore, polynomial terms are joined to the functional expansion that only uses RBF in the approximation functions, ie,

$$u_h(\mathbf{x}) = \sum_{i=1}^{n} R_i(r)\, a_i + \sum_{j=1}^{m} P_j(\mathbf{x})\, b_j = \mathbf{R}^T(r)\,\mathbf{a} + \mathbf{P}^T(\mathbf{x})\,\mathbf{b}, \tag{9}$$

where $u_h(\mathbf{x})$ is the unknown of the problem (for example, velocity or pressure); n and m denote the number of nodes and basis polynomial terms, respectively; and $\mathbf{a}$, $\mathbf{b}$, and $\mathbf{R}(r)$ are defined by the following relations:

$$\begin{aligned} \mathbf{a}^T &= [a_1 \quad a_2 \quad \dots \quad a_n], \mathbf{b}^T = \begin{bmatrix} b_1 & b_2 & \dots & b_m \end{bmatrix} \\ \mathbf{R}^T(r) &= [R_1(r) \quad R_2(r) \quad \dots \quad R_n(r)], \ \mathbf{P}^T(\mathbf{x}) = [P_1(\mathbf{x}) \quad P_2(\mathbf{x}) \quad \dots \quad P_m(\mathbf{x})]. \end{aligned} \tag{10}$$

By substituting the nodal points into Equation (9), the matrix equation can be expressed as follows:

$$\hat{\mathbf{u}} = \mathbf{R}_Q \mathbf{a} + \mathbf{P}_m \mathbf{b}, \tag{11}$$

in which $\mathbf{R}_Q$ and $\mathbf{P}_m$ are written as follows:

$$\mathbf{R}_Q = \begin{bmatrix} R_1(r_1) & \dots & R_n(r_1) \\ \vdots & & \vdots \\ R_1(r_n) & \dots & R_n(r_n) \end{bmatrix}, \mathbf{P}_m = \begin{bmatrix} P_1(\mathbf{x}_1) & \dots & P_m(\mathbf{x}_1) \\ \vdots & & \vdots \\ P_1(\mathbf{x}_n) & \dots & P_m(\mathbf{x}_n) \end{bmatrix}. \tag{12}$$

By substituting $\mathbf{a}$ and $\mathbf{b}$ from relation (13) into Equation (9), it can result to the following relation (for more details, see the works of Hamzehei Javaran and Shojaee[30] and Wang and Liu[34]):

$$\begin{aligned} \mathbf{a} &= \mathbf{S_a}\hat{\mathbf{u}}\ , \quad \mathbf{b} = \mathbf{S_b}\hat{\mathbf{u}} \\ \mathbf{S}_a &= \mathbf{R}_Q^{-1} - \mathbf{R}_Q^{-1}\mathbf{P}_m\mathbf{S}_b, \quad \mathbf{S}_b = \left[\mathbf{P}_m^T\mathbf{R}_Q^{-1}\mathbf{P}_m\right]^{-1}\mathbf{P}_m^T\mathbf{R}_Q^{-1} \end{aligned} \tag{13}$$

$$u_h(\mathbf{x}) = \left[\mathbf{R}^T(r)\,\mathbf{S}_a + \mathbf{P}^T(\mathbf{x})\,\mathbf{S}_b\right]\hat{\mathbf{u}}. \tag{14}$$

By using the aforementioned relation, the nodal values $\hat{\mathbf{u}}$ can be calculated, and the matrix of shape functions is expressed by the following relation:

$$\mathbf{\Phi}(\mathbf{x}) = \mathbf{R}^T(r)\,\mathbf{S}_a + \mathbf{P}^T(\mathbf{x})\,\mathbf{S}_b. \tag{15}$$

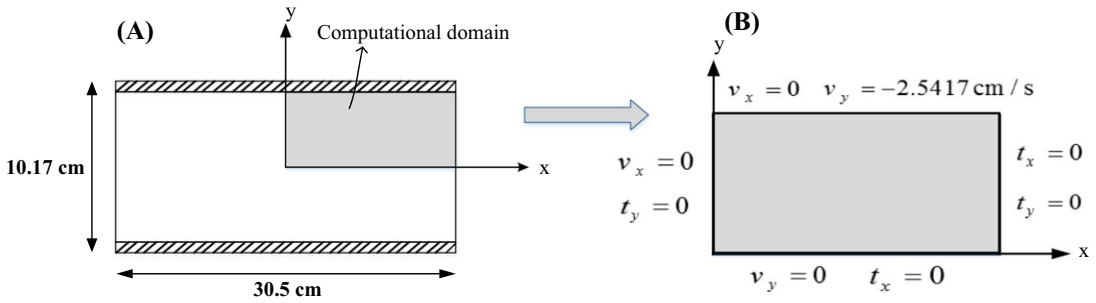

FIGURE 8 The first test. A, The geometry and the computational domain; B, Boundary conditions [Colour figure can be viewed at wileyonlinelibrary.com]

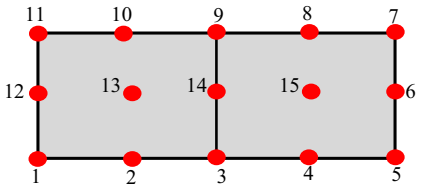

FIGURE 9 The mesh of the first test with 2 elements [Colour figure can be viewed at wileyonlinelibrary.com]

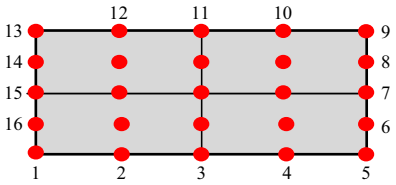

FIGURE 10 The mesh of the first test with 4 elements [Colour figure can be viewed at wileyonlinelibrary.com]

The above approach is used for the 3-node element in a natural coordinate system in the FEM.

The proper RBF is presented by the following relation:

$$R(r) = (\varepsilon r)^{n+1} h_n^{(1)}(\varepsilon r) \qquad \varepsilon > 0, \quad n = 0, 1, 2, \ldots, \tag{16}$$

in which ε and n are the shape parameters of the Hankel RBF and $h_n^{(1)}(\varepsilon r) = \sqrt{\frac{\pi}{2(\varepsilon r)}} H^{(1)}_{n+\frac{1}{2}}(\varepsilon r)$ denotes the spherical Hankel functions of the first kind of order n.

It should be noted that $h_n^{(1)}(\varepsilon r) = j_n(\varepsilon r) + i y_n(\varepsilon r)$ has a strong singularity at its imaginary part. Therefore, the term $(\varepsilon r)^{n+1}$ is used in the proper RBF to resolve this singularity so that the limiting values of the RBF can be calculated as follows:

$$\lim_{r \to 0} (\varepsilon r)^{n+1} h_n^{(1)}(\varepsilon r) = 0 + \frac{(-1)^{n+1} 2^n \sqrt{\pi}}{\Gamma\left(-n + \frac{1}{2}\right)} i. \tag{17}$$

For the 1-dimensional element shown in Figure 3, the vector $\mathbf{R}(r)$ can be written as follows:

$$\mathbf{R}(r) = \begin{bmatrix} R_1(r) \\ R_2(r) \\ R_3(r) \end{bmatrix} = \begin{bmatrix} (\varepsilon |\xi + 1|)^{n+1} h_n^{(1)}(\varepsilon |\xi + 1|) \\ (\varepsilon |\xi|)^{n+1} h_n^{(1)}(\varepsilon |\xi|) \\ (\varepsilon |\xi - 1|)^{n+1} h_n^{(1)}(\varepsilon |\xi - 1|) \end{bmatrix}. \tag{18}$$

It should be noted that, by considering the natural coordinates $[-1,1]$, $|\xi + 1| = 1 + \xi$, $|\xi - 1| = 1 - \xi$ and $|\xi| = \xi\,\text{sgn}(\xi)$ (in which sgn denotes the sign function), and according to the 3-node element shown in Figure 3, the linear field is used for enrichment.

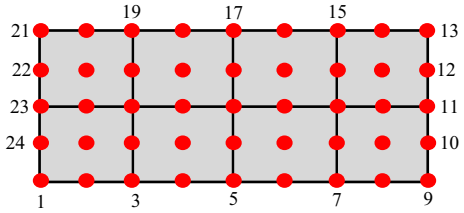

FIGURE 11 The mesh of the first test with 8 elements [Colour figure can be viewed at wileyonlinelibrary.com]

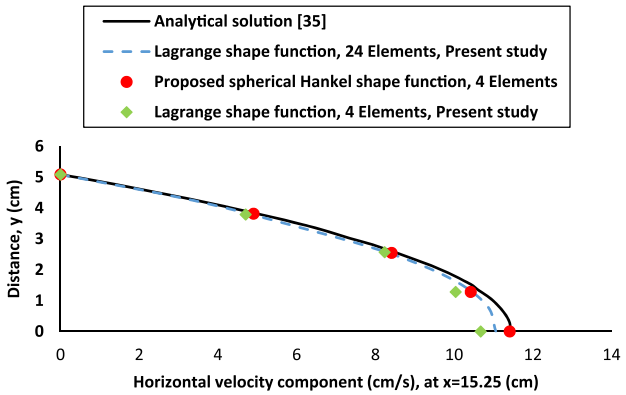

FIGURE 12 The first test. Comparison of the results obtained by classic Lagrange shape functions, spherical Hankel shape functions, and the analytical solution of Nadai[35] for the horizontal velocity component [Colour figure can be viewed at wileyonlinelibrary.com]

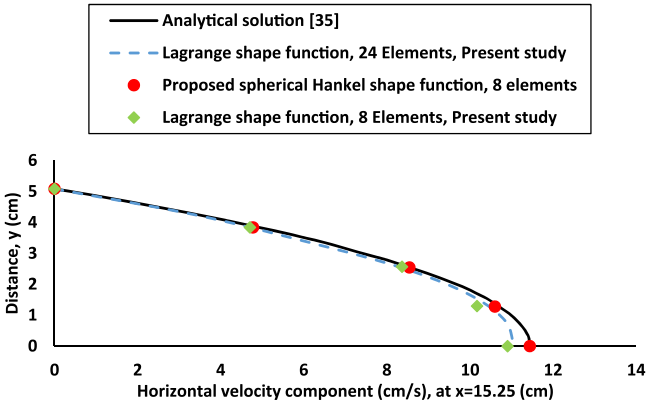

FIGURE 13 The first test. Comparison of the results obtained by classic Lagrange shape functions, spherical Hankel shape functions, and the analytical solution of Nadai[35] for the horizontal velocity component [Colour figure can be viewed at wileyonlinelibrary.com]

The proper vectors and matrices in the enrichment process of Hankel RBF in natural coordinate ξ are written as follows:

$$\mathbf{P}(\xi) = \begin{bmatrix} 1 \\ \xi \end{bmatrix} \tag{19}$$

$$\mathbf{R}_Q = \begin{bmatrix} R_1(r_1) & R_2(r_1) & R_3(r_1) \\ R_1(r_2) & R_2(r_2) & R_3(r_2) \\ R_1(r_3) & R_2(r_3) & R_3(r_3) \end{bmatrix} = \begin{bmatrix} \alpha & \varepsilon^{n+1} h_n^{(1)}(\varepsilon) & (2\varepsilon)^{n+1} h_n^{(1)}(2\varepsilon) \\ & \alpha & \varepsilon^{n+1} h_n^{(1)}(\varepsilon) \\ \text{sym.} & & \alpha \end{bmatrix} \tag{20}$$

$$\mathbf{P}_m = \begin{bmatrix} P_1(\xi_1) & P_2(\xi_1) \\ P_1(\xi_2) & P_2(\xi_2) \\ P_1(\xi_3) & P_2(\xi_3) \end{bmatrix} = \begin{bmatrix} 1 & -1 \\ 1 & 0 \\ 1 & 1 \end{bmatrix}, \tag{21}$$

TABLE 2 The first test. Comparison of the results obtained by classic Lagrange shape functions, spherical Hankel shape functions, and the analytical solution of Nadai[35] for the horizontal velocity component (cm/s) with 2 elements

Node	Classic Lagrange Shape Function (Relative Error, %)	Spherical Hankel Shape Function (Relative Error, %)	Analytical Solution[35]
2	3.1303 (9.47)	2.8848 (0.89)	**2.8594**
3	5.2781 (7.7)	5.7834 (1.13)	**5.7188**
4	9.7253 (13.37)	8.6761 (1.14)	**8.5782**
5	10.0021 (12.55)	11.4376 (0)	**11.4376**
6	8.9343 (4.151)	8.5975 (0.22)	**8.5782**
13	2.0804 (3.0)	2.1381 (0.31)	**2.1447**
14	4.3994 (2.57)	4.2178 (1.66)	**4.2891**
15	6.1560 (4.32)	6.2821 (2.36)	**6.4338**
	L^2 relative error norm = 10.04%	L^2 relative error norm = 1.06%	

TABLE 3 The first test. Comparison of the results obtained by classic Lagrange shape functions, spherical Hankel shape functions, and the analytical solution of Nadai[35] for pressure (N/cm^2) with 2 elements

Node	Classic Lagrange Shape Function (Relative Error, %)	Spherical Hankel Shape Function (Relative Error, %)	Analytical Solution[35]
1	5.8830 (26.4)	5.5324 (18.87)	**4.654125**
3	2.4680 (29.40)	3.6333 (3.93)	**3.4960**
5	2.4895 (---)	1.3333 (---)	**0**
7	0.0529 (89.77)	0.6363 (23.045)	**0.517125**
9	4.512 (12.58)	4.2077 (4.994.1)	**4.00771875**
11	5.8490 (13.11)	5.4515 (5.42)	**5.17125**
	L^2 relative error norm = 35.49%	L^2 relative error norm = 18.73%	

where $\alpha = \lim_{r\to 0} R(r)$, which is formerly bounded by a smoothing trick that leads to having no singularity in $\boldsymbol{R}_Q$. Finally, the shape functions for a 3-node element in the natural coordinate are obtained in the following relation:

$$\begin{aligned}
\boldsymbol{\Phi}(\xi) &= \begin{bmatrix}\phi_1(\xi) & \phi_2(\xi) & \phi_3(\xi)\end{bmatrix} \\
\phi_1(\xi) &= \frac{1}{2}\left(-\xi + \bar{c} + g(\xi)\right) \\
\phi_2(\xi) &= \left(1 - \bar{c}\right) - g(\xi) \\
\phi_3(\xi) &= \frac{1}{2}\left(\xi + \bar{c} + g(\xi)\right),
\end{aligned} \tag{22}$$

where the complex function $g(\xi)$ is expressed as follows:

$$g(\xi) = c\varepsilon^{n+1}\left[|\xi+1|^{n+1}h_n^{(1)}(\varepsilon|\xi+1|) - 2|\xi|^{n+1}h_n^{(1)}(\varepsilon|\xi|) + |\xi-1|^{n+1}h_n^{(1)}(\varepsilon|\xi-1|)\right]. \tag{23}$$

If these new shape functions are compared with the classic Lagrange ones, attractive results are obtained; these are shown in Table 1.

It can be observed that the difference between these 2 shape functions is the function $g(\xi)$. It seems that one of the advantages of proposed shape functions is this additional function because it can be effective in the accuracy and improvement of the results.

Now, the results of a 3-node element are extended to a 9-node one in a 2-dimensional system. The spherical Hankel 9-node element is shown in Figure 4. Then, the shape functions can be easily written as the following relation:

$$\begin{aligned}
&N_1(\xi,\eta) = \phi_1(\xi)\phi_1(\eta), \quad N_2(\xi,\eta) = \phi_1(\xi)\phi_2(\eta), \quad N_3(\xi,\eta) = \phi_1(\xi)\phi_3(\eta) \\
&N_4(\xi,\eta) = \phi_2(\xi)\phi_1(\eta), \quad N_5(\xi,\eta) = \phi_2(\xi)\phi_2(\eta), \quad N_6(\xi,\eta) = \phi_2(\xi)\phi_3(\eta) \\
&N_7(\xi,\eta) = \phi_3(\xi)\phi_1(\eta), \quad N_8(\xi,\eta) = \phi_3(\xi)\phi_2(\eta), \quad N_9(\xi,\eta) = \phi_3(\xi)\phi_3(\eta).
\end{aligned} \tag{24}$$

TABLE 4 The first test. Comparison of the results obtained by classic Lagrange shape functions, spherical Hankel shape functions, and the analytical solution of Nadai[35] for pressure (N/cm^2) with 4 elements

Node	Classic Lagrange Shape Function (Relative Error, %)	Spherical Hankel Shape Function (Relative Error, %)	Analytical Solution[35]
1	5.7330 (23.18)	5.3324 (14.57)	**4.654125**
3	2.7510 (21.31)	3.6043 (3.097)	**3.4960**
5	2.2495 (---)	1.2167 (---)	**0**
9	0.0912 (82.36)	0.6153 (18.98)	**0.517125**
11	4.495 (12.16)	4.1541 (3.65)	**4.00771875**
13	5.7916 (11.99)	5.4012 (4.44)	**5.17125**
	L^2 relative error norm = 31.39%	L^2 relative error norm = 16.27%	

TABLE 5 The first test. Comparison of the results obtained by classic Lagrange shape functions, spherical Hankel shape functions, and the analytical solution of Nadai[35] for pressure (N/cm^2) with 8 elements

Node	Classic Lagrange Shape Function (Relative Error, %)	Spherical Hankel Shape Function (Relative Error, %)	Analytical Solution[35]
1	5.7125 (22.74)	5.2142 (12.03)	**4.654125**
5	2.8013 (19.87)	3.5933 (2.78)	**3.4960**
9	2.2380 (---)	1.2076 (---)	**0**
13	0.0956 (81.51)	0.6048 (16.95)	**0.517125**
17	4.4125 (10.10)	4.1031 (2.324)	**4.00771875**
21	5.71812 (10.57)	5.3186 (2.85)	**5.17125**
	L^2 relative error norm = 30.70%	L^2 relative error norm = 15.38%	

7 | PROPERTIES OF SPHERICAL HANKEL SHAPE FUNCTIONS

7.1 | Kronecker delta property

The Kronecker delta property of the spherical Hankel shape functions can be written in the following form:

$$\phi_m(\xi_n) = \delta_{mn}, \tag{25}$$

where δ_{mn} is the Kronecker symbol. For showing this property, the shape functions are drawn for some cases of shape parameters and indicated in Figures 5, 6 , and 7. It should be noted that the blue, green, and red graphs express functions $\phi_1(\xi)$, $\phi_2(\xi)$, and $\phi_3(\xi)$, respectively, in these Figures.

7.2 | Partition of unity

For a 9-node spherical Hankel element, this property can be easily expressed as follows:

$$\sum_{j=1}^{n} \phi_j(\xi) = 1. \tag{26}$$

7.3 | Linear independence property

The linear independence property of spherical Hankel shape functions can be shown by the following relation:

$$\sum_{m=1}^{n} C_m \phi_m(\xi; \xi_1, \xi_2, \ldots, \xi_n) = 0 \quad \Rightarrow \quad C_k = 0, \quad k = 1, 2, \ldots, n. \tag{27}$$

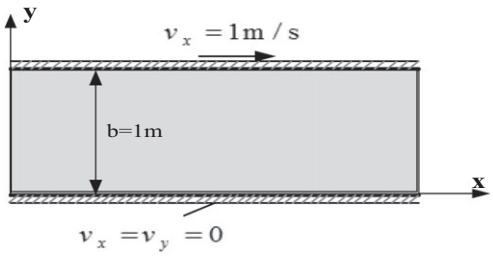

FIGURE 14 The geometry and boundary conditions for the second test

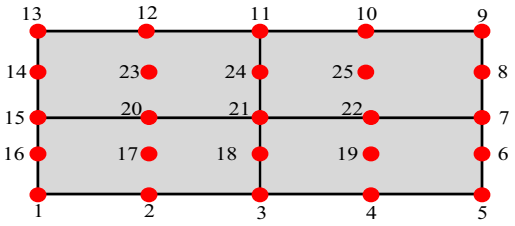

FIGURE 15 The mesh of the second test with 4 elements [Colour figure can be viewed at wileyonlinelibrary.com]

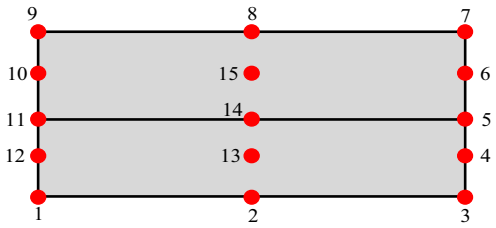

FIGURE 16 The mesh of the second test with 2 elements [Colour figure can be viewed at wileyonlinelibrary.com]

By substituting $\xi = \xi_k$ into the aforementioned relation and the Kronecker delta property, the linear independence can be written as follows:

$$0 = \sum_{m=1}^{n} C_m \phi_m(\xi_k) = \sum_{m=1}^{n} C_m \delta_{mk} = C_k \quad \rightarrow \quad C_k = 0, \quad k = 1, 2, \ldots, n. \tag{28}$$

7.4 | Infinite piecewise continuity

For a 3-node Hankel element, the nth-order derivative of the proposed shape functions can be expressed as follows.

$$\begin{array}{lll}
\phi_1(\xi) = \frac{1}{2}\left(-\xi + \bar{c} + g(\xi)\right) & \phi_2(\xi) = \left(1 - \bar{c}\right) - g(\xi) & \phi_3(\xi) = \frac{1}{2}\left(\xi + \bar{c} + g(\xi)\right) \\
\phi_1'(\xi) = \frac{1}{2}\left(-1 + g'(\xi)\right) & \phi_2'(\xi) = -g'(\xi) & \phi_3'(\xi) = \frac{1}{2}\left(1 + g'(\xi)\right) \\
\phi_1''(\xi) = \frac{g''(\xi)}{2} & \phi_2''(\xi) = -g''(\xi) & \phi_3''(\xi) = \frac{g''(\xi)}{2} \\
\phi_1'''(\xi) = \frac{g'''(\xi)}{2} & \phi_2'''(\xi) = -g'''(\xi) & \phi_3'''(\xi) = \frac{g'''(\xi)}{2} \\
\vdots & \vdots & \vdots
\end{array} \tag{29}$$

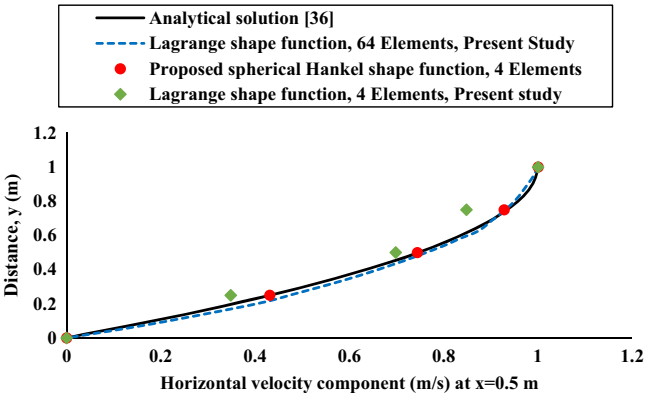

FIGURE 17 The second test. Comparison of the results obtained by classic Lagrange shape functions, spherical Hankel shape functions, and the analytical solution of Reddy[36] for the horizontal velocity component [Colour figure can be viewed at wileyonlinelibrary.com]

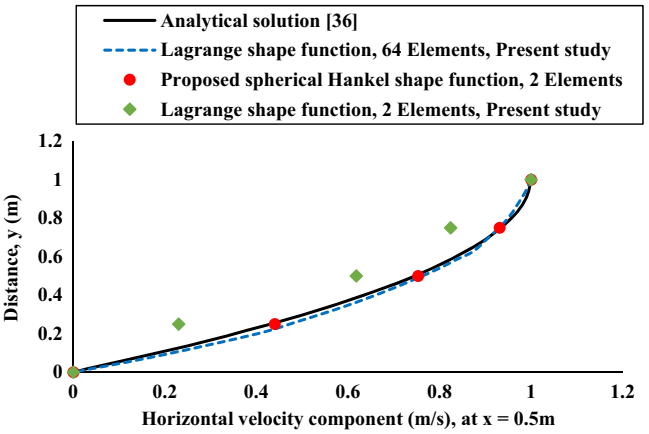

FIGURE 18 The second test. Comparison of the results obtained by classic Lagrange shape functions, spherical Hankel shape functions, and the analytical solution of Reddy[36] for the horizontal velocity component [Colour figure can be viewed at wileyonlinelibrary.com]

According to the feature of spherical Hankel shape functions, a recurrence relation is established between the derivatives of these functions by the following equation:

$$\left(\frac{d}{xdx}\right)^{p}\left[x^{n+1}h_{n}^{(1)}(x)\right]=x^{n-p+1}h_{n-p}^{(1)}(x)\,. \tag{30}$$

For instance, up to the third derivative of $g(\xi)$ are given by the following relations:

$$\begin{aligned}
g(\xi)&=c\varepsilon^{n+1}\left[(1+\xi)^{n+1}h_{n}^{(1)}(\varepsilon(1+\xi))-2|\xi|^{n+1}h_{n}^{(1)}(\varepsilon|\xi|)+(1-\xi)^{n+1}h_{n}^{(1)}(\varepsilon(1-\xi))\right]\\
g'(\xi)&=c\varepsilon^{n+2}\left[(1+\xi)^{n+1}h_{n-1}^{(1)}(\varepsilon(1+\xi))-2(H(\xi)-H(-\xi))|\xi|^{n+1}h_{n-1}^{(1)}(\varepsilon|\xi|)-(1-\xi)^{n+1}h_{n-1}^{(1)}(\varepsilon(1-\xi))\right]\\
g''(\xi)&=c\Big\{\varepsilon^{n+3}\left[(1+\xi)^{n+1}h_{n-2}^{(1)}(\varepsilon(1+\xi))-2(H(\xi)+H(-\xi))|\xi|^{n+1}h_{n-2}^{(1)}(\varepsilon|\xi|)+(1-\xi)^{n+1}h_{n-2}^{(1)}(\varepsilon(1-\xi))\right]\\
&\quad+\varepsilon^{n+2}\left[(1+\xi)^{n}h_{n-1}^{(1)}(\varepsilon(1+\xi))-2(H(\xi)+H(-\xi))|\xi|^{n}h_{n-1}^{(1)}(\varepsilon|\xi|)+(1-\xi)^{n}h_{n-1}^{(1)}(\varepsilon(1-\xi))\right]\Big\}\\
g'''(\xi)&=c\Big\{\varepsilon^{n+4}\left[(1+\xi)^{n+1}h_{n-3}^{(1)}(\varepsilon(1+\xi))-2(H(\xi)-H(-\xi))|\xi|^{n+1}h_{n-3}^{(1)}(\varepsilon|\xi|)-(1-\xi)^{n+1}h_{n-3}^{(1)}(\varepsilon(1-\xi))\right]\\
&\quad+3\varepsilon^{n+3}\left[(1+\xi)^{n}h_{n-2}^{(1)}(\varepsilon(1+\xi))-2(H(\xi)-H(-\xi))|\xi|^{n}h_{n-2}^{(1)}(\varepsilon|\xi|)-(1-\xi)^{n}h_{n-2}^{(1)}(\varepsilon(1-\xi))\right]\Big\},
\end{aligned} \tag{31}$$

where H denotes the famous Heaviside step function. Note that Equation (31) can be extended for a 9-node element.

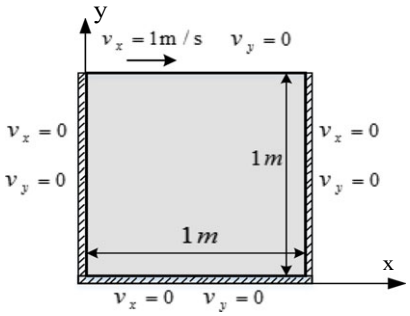

FIGURE 19 The geometry and boundary conditions for the third test

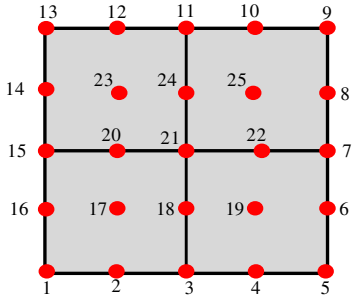

FIGURE 20 The mesh of the third test with 4 elements [Colour figure can be viewed at wileyonlinelibrary.com]

8 | BENCHMARKS TESTS

In this part, to show the efficiency and accuracy of the proposed method, 4 numerical tests are studied for the incompressible viscous flow problems, and at the end of each example, the results of the proposed method are compared with the classic finite element and the analytical and/or numerical solutions. In addition, for the values of each table, the relative error and also the L^2 relative error norm are calculated. These errors are computed by relations (32) and (33).

$$\text{Relative error} = \frac{|u_e - u_c|}{|u_e|} \tag{32}$$

$$\text{L}^2\,\text{Relative error norm} = \sqrt{\frac{\sum_{i=1}^{n} (u_e(i) - u_c(i))^2}{\sum_{i=1}^{n} u_e(i)^2}}. \tag{33}$$

It should be noted that, for these examples, the 9-node Hankel element is used.

8.1 | Fluid squeezed between parallel plates

In this problem, an incompressible viscous fluid between 2 parallel plates, which move toward each other with the velocity of 2.5417 cm/s, with the steady slow flow is considered. The length and distance of the 2 plates are considered 30.5 cm and 10 cm, respectively. Owning to the symmetry, just a quadrant of the domain is considered. Figure 8 shows the geometry, the computational domain, and the boundary conditions of the first test. The viscosity is considered 0.6895 N·s/cm^2 and, due to the slow flow between the parallel plates, the convective terms in the Navier-Stokes equations are neglected. For the analysis of this problem, 2, 4, and 8 quadratic 9-node elements are used in the present model and shown in Figure 9, Figure 10, and Figure 11, respectively. The comparison of the results of the proposed method, the classic finite element, and the analytical solution of Nadai[35] is shown in Figures 12 and 13 and Tables 2 to 5 for the velocity and pressure field. It should be noted that the results for 4- and 8-element meshes are compared with the 24-element meshes in addition to the analytical solution (Figures 12 and 13).

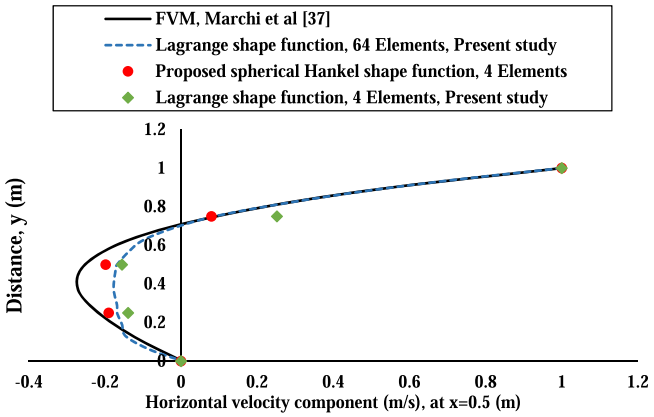

FIGURE 21 The third test. Comparison of the results obtained by classic Lagrange shape functions, spherical Hankel shape functions, and the numerical solution of Marchi et al[37] for the horizontal velocity component (Re = 1). FVM, finite volume method [Colour figure can be viewed at wileyonlinelibrary.com]

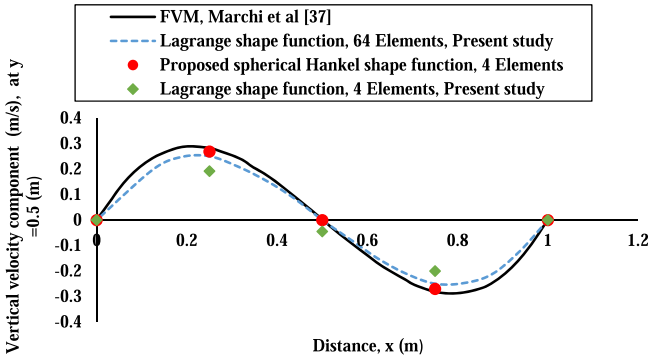

FIGURE 22 The third test. Comparison of the results obtained by classic Lagrange shape functions, spherical Hankel shape functions, and the numerical solution of Marchi et al[37] for the vertical velocity component (Re = 1). FVM, finite volume method [Colour figure can be viewed at wileyonlinelibrary.com]

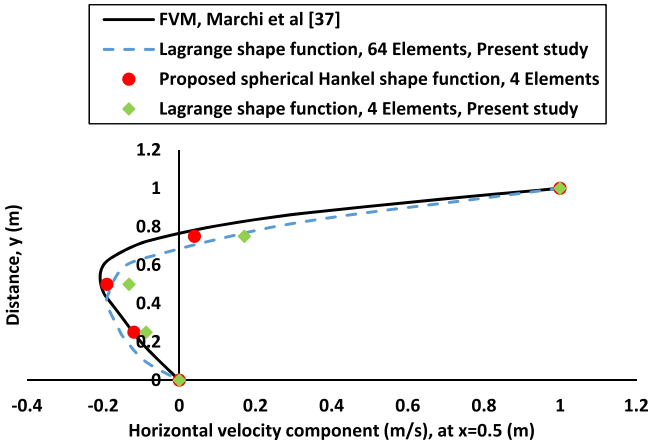

FIGURE 23 The third test. Comparison of the results obtained by classic Lagrange shape functions, spherical Hankel shape functions, and the numerical solution of Marchi et al[37] for the vertical velocity component (Re = 10). FVM, finite volume method [Colour figure can be viewed at wileyonlinelibrary.com]

According to the Figures and Tables, it is clear that, using the proposed method (eg, employing spherical Hankel shape functions) with a few number of elements, the results become closer to the analytical solution of Nadai[35] in comparison with the classic FEM (classic Lagrange shape functions). In other words, the computational error of the proposed method is less than the classic FEM. In addition, by considering the Figures and the calculated errors (relative error and L^2 relative error norm) in the Tables, it can be found that, by refined meshes (4- and 8-element meshes), the accuracy of the results is increased.

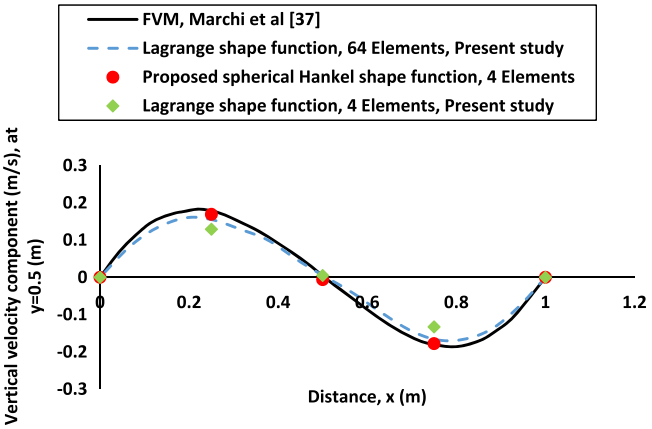

FIGURE 24 The third test. Comparison of the results obtained by classic Lagrange shape functions, spherical Hankel shape functions, and the numerical solution of Marchi et al[37] for the vertical velocity component (Re = 10). FVM, finite volume method [Colour figure can be viewed at wileyonlinelibrary.com]

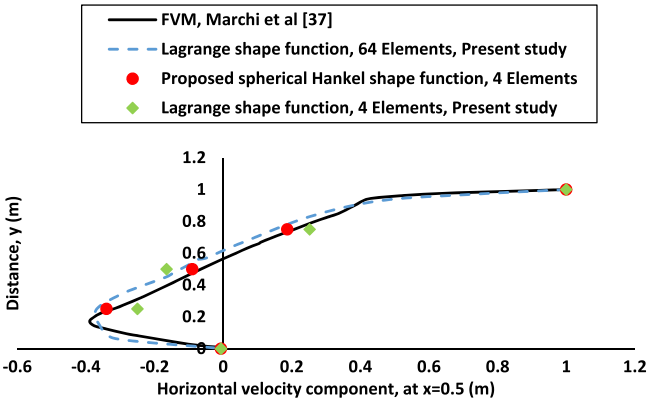

FIGURE 25 The third test. Comparison of the results obtained by classic Lagrange shape functions, spherical Hankel shape functions, and the numerical solution of Marchi et al[37] for the horizontal velocity component (Re = 1000). FVM, finite volume method [Colour figure can be viewed at wileyonlinelibrary.com]

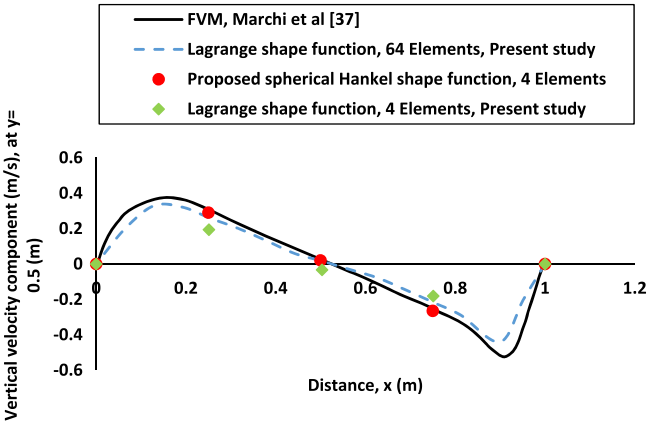

FIGURE 26 The third test. Comparison of the results obtained by classic Lagrange shape functions, spherical Hankel shape functions, and the numerical solution of Marchi et al[37] for the vertical velocity component (Re = 1000). FVM, finite volume method [Colour figure can be viewed at wileyonlinelibrary.com]

8.2 | Couette flow

This test is a channel with 2 parallel flat walls where a viscous incompressible fluid flows between them. If the top wall has a velocity in the *x*-direction, the flow is called *Couette flow*, and if it is fixed, the flow is named the Poiseuille flow.[36]

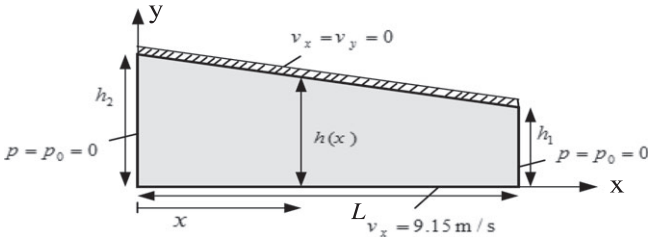

FIGURE 27 The geometry and boundary conditions for the fourth test

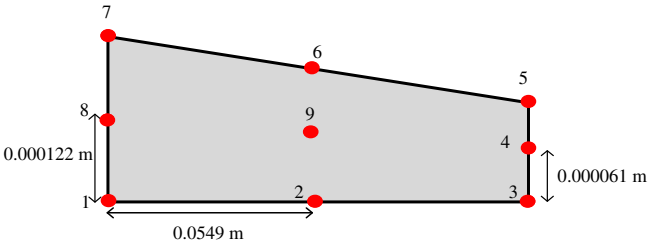

FIGURE 28 The mesh of the fourth test with 1 element [Colour figure can be viewed at wileyonlinelibrary.com]

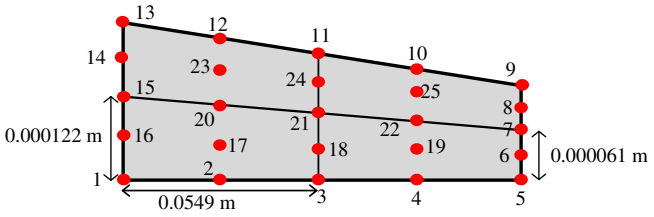

FIGURE 29 The mesh of the fourth test with 4 elements [Colour figure can be viewed at wileyonlinelibrary.com]

In this test, the top wall moves with a velocity of 1 m/s in the *x*-direction (Couette flow) and the viscosity is considered 1 Pa·s. The geometry and boundary conditions of the test are shown in Figure 14.

The governing equation is obtained of Navier-Stokes equations as follows:

$$\mu \frac{d^2 v_x}{dy^2} = \frac{dp}{dx}. \tag{34}$$

First, the computational domain is divided into 4 elements and, then, into 2 elements. The mesh geometries are shown in Figures 15 and 16. Then, the velocity field is plotted at x = 0.5 m using the classic finite element and the new method with proposed shape functions and is compared with the analytical solution of Reddy[36] in Figures 17 and 18.

It is observed that the results of the proposed method (with just 4 and 2 elements) have a good adaptation with the analytical solution of Reddy,[36] compared with the results of the classic FEM.

8.3 | Lid-driven cavity flow

The third test is a viscous and incompressible fluid with laminar flow in a square cavity (classical cavity flow problem). The bottom, left, and right walls are fixed, and the top wall moves toward the right with $v_x = 1$ m/s. The geometry and boundary conditions are shown in Figure 19.

In this test, the results are obtained with the grid with 64 and 4 elements using the classic finite element and the proposed method. The mesh with 4 elements is shown in Figure 20. The Reynolds number (Re) is defined by relation (35), and the results are presented for the velocity in the *x*-direction at x = 0.5 m and the velocity in the *y*-direction at y = 0.5 m for the different Reynolds number.

$$\mathrm{Re} = \rho U \frac{a}{\mu}. \tag{35}$$

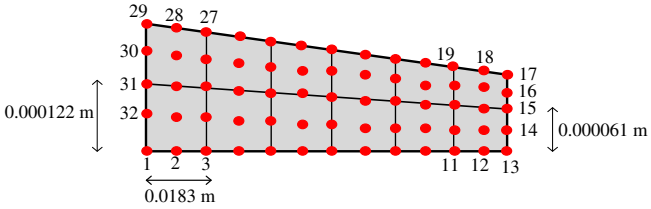

FIGURE 30 The mesh of the fourth test with 12 elements [Colour figure can be viewed at wileyonlinelibrary.com]

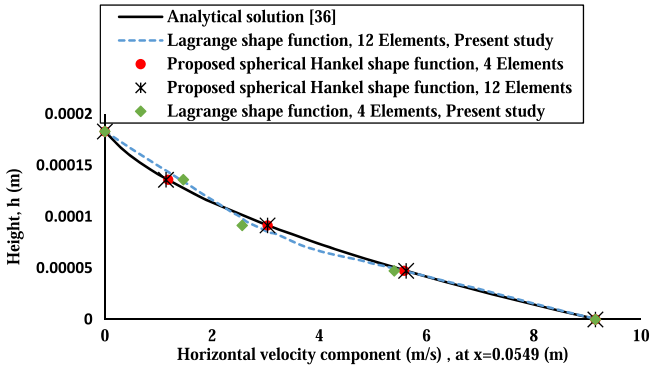

FIGURE 31 The fourth test. Comparison of the results obtained by classic Lagrange shape functions, spherical Hankel shape functions, and the analytical solution of Reddy[36] for the horizontal velocity component [Colour figure can be viewed at wileyonlinelibrary.com]

In relation (35), U is the velocity of the top wall in the x-direction and a indicates the dimension of cavity that is equal to unit. By putting the values of Reynolds numbers in the aforementioned relation, the viscosity is obtained and the Navier-Stokes equations can be solved.

Figures 21 to 26 indicate the results of the classic and present method comparing with the numerical solution of Marchi et al.[37]

As it can be observed from the Figures, for different Reynolds numbers, the results of the spherical Hankel shape functions with 4 elements are close to the numerical solution of Marchi et al[37] comparing with the classic finite element with 64 and 4 elements.

8.4 | Viscous lubricant flow in a slider bearing

The last test case is a slider bearing that includes 2 pads. The bottom pad moves with $v_x = 9.15$ m/s with respect to the top pad. In this test, the top plate has a small angle with respect to the horizontal axis and it is fixed. The space between 2 pads is filled with a lubricant. The beginning and end of the bearing are open, and therefore, the pressure is atmospheric p_0. The geometry and the boundary conditions are shown in Figure 27.

The viscosity is assumed $\mu = 0.0383$ N·s/m^2. In addition, $h_1 = 2.44 \times 10^{-4}$ m, $h_2 = 1.22 \times 10^{-4}$ m, and $L = 0.1098$ m. It should be noted that the distance of 2 pads is small, and then, it is assumed that $v_y = 0$. The flow has a 2-dimensional state, and the governing equation can be written as follows[36]:

$$\mu \frac{d^2 v_x}{dy^2} = \frac{dp}{dx}. \tag{36}$$

The results are obtained for a grid with 1, 4, and 12 elements and are compared with the results of the classic finite element and the analytical solution of Reddy.[36] The mesh with 1, 4, and 12 elements for this test is shown in Figures 28 to 30. In addition, the results of velocity and pressure are presented in Figure 31 and Tables 6 to 8 .

According to Figure 31 and Table 6 and by comparing the results with the analytical solution, it can be found that the new method presents very accurate results with 4 and 12 elements with respect to the classic method for the velocity field. In addition, the results of the proposed method with 1 spherical Hankel element are presented in Tables 7 and 8.

The analysis of the results of Tables 7 and 8 shows the high accuracy and robustness of the proposed method.

TABLE 6 The fourth test. Comparison of the results obtained by classic Lagrange shape functions, spherical Hankel shape functions, and the analytical solution of Reddy[36] for pressure (Pa) with 4 elements

Node	Classic Lagrange Shape Function (Relative Error, %)	Spherical Hankel Shape Function (Relative Error, %)	Analytical Solution[36]
3	6081.014×10^2 (5.83)	5976.68×10^2 (4.01)	5745.84×10^2
11	5999.6625×10^2 (4.42)	5971.843×10^2 (3.93)	5745.84×10^2
21	5976.6791×10^2 (4)	5953.734×10^2 (3.62)	5745.84×10^2
	L^2 relative error norm = 4.82%	L^2 relative error norm = 3.86%	

TABLE 7 The fourth test. Comparison of the results obtained by classic Lagrange shape functions, spherical Hankel shape functions, and the analytical solution of Reddy[36] for the horizontal velocity component (m/s) with 1 element

Node	Classic Lagrange Shape Function (Relative Error, %)	Spherical Hankel Shape Function (Relative Error, %)	Analytical Solution[36]
4	6.7923 (1.02)	6.81 (0.76)	**6.8625**
8	2.138 (6.53)	2.2658 (0.95)	**2.2875**
9	2.5315 (17)	3.0256 (0.8)	**3.05**
	L^2 relative error norm = 6.93%	L^2 relative error norm = 0.7876%	

TABLE 8 The fourth test. Comparison of the results obtained by classic Lagrange shape functions, spherical Hankel shape functions, and the analytical solution of Reddy[36] for pressure (Pa) with 1 element

Node	Classic Lagrange Shape Function (Relative Error, %)	Spherical Hankel Shape Function (Relative Error, %)	Analytical Solution[36]
2	6172.001×10^2 (7.42)	5990.35×10^2 (4.25)	5745.84×10^2
6	6004.6615×10^2 (4.5)	5989.941×10^2 (4.25)	5745.84×10^2
9	5996.9841×10^2 (4.38)	5966.416×10^2 (3.84)	5745.84×10^2
	L^2 relative error norm = 5.61%	L^2 relative error norm = 4.12%	

9 | CONCLUSION

In this research, new spherical Hankel shape functions for the FEM in solving 2-dimensional viscous incompressible flow problems have been developed. To approximate the hydrodynamic variables (such as velocity and pressure), the FEM with the classic Lagrange and spherical Hankel shape functions was used. The new shape functions were derived using the first and second kind of Bessel functions. For the enrichment of Hankel RBFs, polynomial terms were joined to the functional expansion that only uses spherical Hankel RBF in the approximation. Therefore, the accuracy in the interpolation to approximate the variables was increased. This new formulation was examined by 4 benchmark tests. Then, the results were compared with the available analytical solution. With the analysis of the present model results, it was found that the new spherical Hankel shape functions with fewer number of elements have the capability to improve the accuracy of the results in comparison with the classic finite element results.

ORCID

Mahnaz Ghaeini-Hessaroeyeh http://orcid.org/0000-0003-1418-1538

REFERENCES

1. Reddy JN. *An Introduction to Nonlinear Finite Element Analysis*. New York: Oxford University Press Inc; 2004.
2. Zienkiewicz OC. *The Finite Element Method in Engineering Science*. New York: McGraw-Hill; 1971.
3. Hood P. A Finite Element Solution of the Navier-Stokes Equations for Incompressible Contained Flow [MSc thesis]. Swansea, Wales: University of Wales; 1970.
4. Oden JT. The Finite Element Method In Fluid Mechanics. *Lecture for NATO Advanced Study Institute on Finite Element Methods in Continuum Mechanics*. Lisbon, Portugal; 1971.
5. Taylor C, Hood P. A numerical solution of the Navier-Stokes equations using the finite element technique. *Comput Fluids*. 1973;1:73-100.
6. Hughes T, Liu WK, Brooks A. Finite element analysis of incompressible viscous flows by the penalty function formulation. *J Comput Phys*. 1979;30:1-60.
7. Souli M, Zolesio JP. Finite element method for free surface flow problems. *Comput Methods Appl Mech Eng*. 1996;129:43-51.
8. Ding Y, Kawahara M. Three-dimensional linear stability analysis of incompressible viscous flows using the finite element method. *Int J Numer Methods Fluids*. 1999;31:451-479.
9. Basa M, Quinlan N, Lastiwka M. Robustness and accuracy of SPH formulations for viscous flow. *Int J Numer Methods Fluids*. 2009;60:1127-1148.
10. You C, Qiu Y, Xu X, Xu D. Numerical simulations of viscous flows using a meshless method. *Int J Numer Methods Fluids*. 2008;58:727-741.
11. Buhmann MD. *Radial Basis Functions: Theory and Implementations*. Vol 12. Cambridge, UK: Cambridge University Press; 2003.
12. Farcas A, Elliott L, Ingham DB, Lesnic D. The dual reciprocity boundary element method for solving Cauchy problems associated to the Poisson equation. *Eng Anal Bound Elem*. 2003;27:955-962.
13. Brebbia CA, Nardini D. Dynamic analysis in solid mechanics by an alternative boundary elements procedure. *Int J Soil Dyn Earthquake Eng*. 1983;2:228-233.
14. Golberg MA, Chen CS. The theory of radial basis functions applied to the BEM for inhomogeneous partial differential equations. *Bound Elem Commun*. 1994;5:57-61.
15. Agnantiaris JP, Polyzos D, Beskos DE. Some studies on dual reciprocity BEM for elastodynamic analysis. *Comput Mech*. 1996;17:270-277.
16. Chen CS. The method of fundamental solution for non-linear thermal explosions. *Commun Numer Methods Eng*. 1995;11:675-681.
17. Karur SR, Ramachandran PA. Augmented thin plate spline approximation in DRM. *Bound Elem Commun*. 1995;6:55-58.
18. Rashed YF. Transient dynamic boundary element analysis using Gaussian-based mass matrix. *Eng Anal Bound Elem*. 2002;26:265-279.
19. Agnantiaris JP, Polyzos D, Beskos DE. Free vibration analysis of nonaxisymmetric and axisymmetric structures by the dual reciprocity BEM. *Eng Anal Bound Elem*. 2001;25:713-723.
20. Samaan MF, Rashed YF. BEM for transient 2D elastodynamics using multiquadric functions. *Int J Solids Struct*. 2007;44:8517-8531.
21. Hamzehei Javaran S, Khaji N. Inverse multiquadric (IMQ) function as radial basis function for plane dynamic analysis using dual reciprocity boundary element method. Paper presented at: 15th World Conference on Earthquake Engineering; 2012; Lisbon, Portugal.
22. Chen CS, Brebbia CA, Power H. Dual reciprocity method using compactly supported radial basis functions. *Commun Numer Methods Eng*. 1999;15:137-150.
23. Golberg MA, Chen CS, Ganesh M. Particular solutions of 3D Helmholtz-type equations using compactly supported radial basis functions. *Eng Anal Bound Elem*. 2000;24:539-547.
24. Rashed YF. BEM For dynamic analysis using compact supported radial basis functions. *Comput Struct*. 2002;80:1351-1367.
25. Samaan MF, Rashed YF, Ahmed MA. The dual reciprocity method applied to free vibrations of 2D structures using compact supported radial basis functions. *Comput Mech*. 2007;41:85-106.
26. Hamzeh Javaran S, Khaji N, Moharrami H. A dual reciprocity BEM approach using new Fourier radial basis functions applied to 2D elastodynamic transient analysis. *Eng Anal Bound Elem*. 2011;35:85-95.
27. Khaji N, Hamzehei Javaran S. New complex Fourier shape functions for the analysis of two-dimensional potential problems using boundary element method. *Eng Anal Bound Elem*. 2013;37:260-272.
28. Hamzehei Javaran S, Khaji N. Dynamic analysis of plane elasticity with new complex Fourier radial basis functions in the dual reciprocity boundary element method. *App Math Model*. 2014;38:3641-3651.
29. Hamzeh Javaran S, Khaji N, Noorzad A. First kind Bessel function (J-Bessel) as radial basis function for plane dynamic analysis using dual reciprocity boundary element method. *Acta Mechanica*. 2011;218:247-258.
30. Hamzehei Javaran S, Shojaee S. The solution of elasto static and dynamic problems using the boundary element method based on spherical Hankel element framework. *Int J Numer Methods Eng*. 2017;112(13):2067-2086. https://doi.org/10.1002/nme.5595
31. Reddy JN. *The Finite Element Method in Heat Transfer and Fluid Dynamics*. Third Edition. Boca Raton, FL: CRC Press; 2010.
32. Reddy JN. *Applied Functional Analysis and Variational Methods in Engineering*. New York: McGraw-Hill; 1986. Reprinted by Krieger Publishing, Melbourne, FL; 1991.
33. Oden JT, Carey GF. *Finite Elements: Mathematical Aspects*. Vol IV. Englewood Cliffs, NJ: Prentice Hall; 1983.
34. Wang JG, Liu GR. On the optimal shape parameters of radial basis functions used for 2-D meshless methods. *Comput Methods Appl Mech Eng*. 2002;191:2611-2630.

35. Nadai A. *Theory of Flow and Fracture of Solids*. New York: McGraw-Hill; 1963.
36. Reddy JN. *An Introduction to Continuum Mechanics*. Cambridge, UK: Cambridge University Press; 2013.
37. Marchi CH, Suero R, Araki LK. The lid-driven square cavity flow: numerical solution with a 1024 x 1024 grid. *J Braz Soc Mech Sci Eng*. 2009;31:186-198.

How to cite this article: Farmani S, Ghaeini-Hessaroeyeh M, Javaran SH. The improvement of numerical modeling in the solution of incompressible viscous flow problems using finite element method based on spherical Hankel shape functions. *Int J Numer Meth Fluids*. 2018;87:70–89. https://doi.org/10.1002/fld.4482